

Mechanistic study of mixed lithium halides solid state electrolytes

Davide Tisi,¹ Sergey Pozdnyakov,¹ and Michele Ceriotti^{1,*}

¹Laboratory of Computational Science and Modeling, Institut des Matériaux,
École Polytechnique Fédérale de Lausanne, 1015 Lausanne, Switzerland

(Dated: November 20, 2025)

Lithium halides with the general formula $\text{Li}_x\text{M}_y\text{X}_6$, where M indicates transition metal ions and X halide anions are very actively studied as solid-state electrolytes, because of relatively low cost, high stability and Li conductivity. The structure and properties of these halide-based solid electrolytes (HSE) can be tuned by alloying, e.g. using different halides and/or transition metals simultaneously. The large chemical space is difficult to sample by experiments, making simulations based on broadly applicable machine-learning interatomic potentials (MLIPs) a promising approach to elucidate structure-property relations, and facilitate the design of better-performing compositions. Here we focus on the $\text{Li}_3\text{YCl}_{6x}\text{Br}_{6(1-x)}$ system, for which reliable experimental data exists, and use the recently-developed PET-MAD universal MLIP to investigate the structure of the alloy, the interplay of crystalline lattice, volume and chemical composition, and its effect on Li conductivity. We find that the distribution of Cl and Br atoms is only weakly correlated, and that the primary effect of alloying is to modulate the lattice parameter – although it can also trigger transition between different lattice symmetries. By comparing constant-volume and constant-pressure simulations, we disentangle the effect of lattice parameter and chemical composition on the conductivity, finding that the two effects compensate each other, reducing the overall dependency of conductivity on alloy composition. We also study the effect of Y-In metal substitution finding a small increase in the conductivity for the C2/m phase at 25% In content, and an overall higher conductivity for the P $\bar{3}$ m1 phase.

I. INTRODUCTION

All-solid-state batteries (ASSBs) are at the center of scientific investigation as the principal power source for next-generation electric vehicles (EVs)^{1,2}. Compared to conventional batteries, ASSBs swap highly flammable liquid electrolytes for much safer solid-state electrolytes (SSEs), which potentially enable shorter charging times without electrolyte polarization³ and much higher energy density⁴. Among the many classes of SSE, the halide-based solid electrolytes (HSE), with general formula of Li_3MX_6 (M = In, Y, Sc, or Er, etc., X = Cl or Br), have gained more and more interest^{5–11} thanks to a combination of high ionic conductivity, relatively low production cost and good air/moisture stability with respect to other classes of SSE such as sulfides and oxides. HSE have been studied for almost 30 years as a possible choice for SSE, but they became popular in 2018 when Asano and collaborators⁸ used different synthesis methods to obtain two compounds with high room temperature (RT) ionic conductivity: 0.051 S/m for Li_3YCl_6 , and 0.17 S/m for Li_3YBr_6 . This work sparked an interest in halide-based SSE and showed that the use of different halogens can significantly affect conductivity and structure. In particular, Li_3YCl_6 was found in the trigonal (P $\bar{3}$ m1) phase while Li_3YBr_6 was in the monoclinic (C2/m) structure. Different experiments agree that Li_3YBr_6 has higher conductivity than Li_3YCl_6 , but they disagree on the effect of alloying. van der Maas *et al.*¹² finds an increase of conductivity upon doping Li_3YCl_6 with Br in the P3m1 symmetry, and that Li_3YBr_6 has the highest conductivity at a low level of Cl doping. They also reports a considerably higher conductivity for Li_3YBr_6 (0.47 S/m) than the

one obtained by Asano *et al.*⁸. Liu *et al.*¹³, instead, finds an increase in conductivity for the 1:1 alloy $\text{Li}_3\text{YBr}_3\text{Cl}_3$, that maintains a C2/m symmetry.

Despite the experimental evidence of the importance of the halogen substitution, detailed computational studies of its effect on conductivity are lacking, mainly because most studies rely on density functional theory (DFT) to obtain an accurate description of the SSE's properties^{14–17}. Quantum mechanical approaches are quite accurate and can provide insightful evidence of relevant effects^{16,18–20}, but they are burdened by a high computational cost that limits their applicability to small systems not suited to capture the study of the disorder that can arise from the substitution of halogen atoms. To address this cost/accuracy tradeoff one can use machine learning interatomic potentials (MLIPs), which, once properly trained over accurate quantum mechanical data, have the accuracy of DFT at a cost only marginally higher than classical force fields^{21–33}. Accurate MLIPs can be used to study the conduction properties of SSE^{34–43} but they have traditionally relied on the availability of an accurate and dedicated training dataset, which can be complicated to generate and can require significant computational effort, in particular for chemically diverse compounds such as $\text{Li}_x\text{M}_y\text{X}_6$. In recent years, so-called universal MLIPs^{44–47} have been constructed by training on a large dataset⁴⁸ that spans the whole periodic table. These potentials are capable of providing (semi)quantitative results in principle, out-of-the-box, without the need for further training, or with minimal fine-tuning on a small dataset for specific applications.

In this work, we study the effects of alloying on

the structures, phase stability and conductivity of $\text{Li}_3\text{YCl}_{6x}\text{Br}_{6(1-x)}$ using a universal potential, called PET-MAD, which is based on the Point Edge Transformer (PET) architecture⁴⁹ trained on the Massive Atomic Diversity (MAD) dataset⁴⁸.

II. METHODS

A. Universal potential and model architecture

The calculations in this work are made with MLIPs based on the Point Edge Transformer (PET) architecture⁴⁹, a graph neural network (GNN) that has demonstrated state-of-the-art accuracy on diverse molecular and materials benchmarks. At each message-passing layer l , PET maintains and refines feature vectors, or messages, $f_{ij}^l \in \mathbb{R}^{d_{\text{PET}}}$ associated with each ordered pair of atoms i, j within the specified cutoff distance, and where d_{PET} is the embedding dimension chosen as hyperparameter. These messages are updated by an arbitrarily deep transformer^{50,51}, applied independently to the neighborhood of every central atom i . For atom i at layer l , the transformer (shared across central atoms i and unique for each GNN layer l) takes the collection of incoming messages $\{f_{ji}^l\}_j$ from all neighbors j as input tokens, performs a permutationally covariant sequence-to-sequence transformation, and returns the set of outgoing messages $\{f_{ij}^{l+1}\}_j$ from the central atom to all the neighbors. The target property, such as potential energy, is obtained by applying feed-forward neural networks to representations f_{ij}^l and summing all the contributions over bonds and layers. The base PET model, unlike other common frameworks^{22,23,25,52,53}, operates directly on the Cartesian coordinates of the neighbors, avoiding the need for a symmetric invariant (or equivariant) descriptor, which, in turn, leads to a favorable balance between model expressivity and computational cost. Rotational invariance is learned during training through data augmentations. Recent work from Langer *et al.*⁵⁴ showed that not-symmetrized PET can learn rotational symmetry and accurately predict observables to a very high degree of rotational equivariance.

To use a potential that could handle the large chemical diversity typical of these materials, we used the newly developed universal machine learning potential PET-MAD⁴⁷. It is a model based on the PET architecture, trained over the Massive Atomic Diversity (MAD) dataset⁴⁸, which consists of 95595 structures, containing 85 elements in total (with atomic numbers ranging from 1 to 86, excluding Astatine). PET-MAD proved to be sufficiently accurate to allow direct application to a variety of different systems, including SSE⁴⁷. To validate the capability of our potential on describing halides SSE, we also fine-tuned the model on a dataset of halides SSE.

B. Training set construction and validation of the ML models

We construct the training set for the ML models in an iterative fashion. We explored the configurational space of Li_3YBr_6 and Li_3YCl_6 using the universal potential to generate structures. Then we randomly substituted some Br atoms with Cl and vice versa to completely explore the chemical space. To evaluate reference energetics for the specific dataset, we used the same parameters used for PET-MAD, to keep the fine-tuning empirically consistent. The MAD dataset, as reported in Ref.⁴⁸, is constructed using the Quantum Espresso v7.2 package^{55–58}, using the PBEsol exchange-correlation functional⁵⁹, which has good accuracy for solids, and the standard solid-state pseudopotential library (SSSP) v1.2 (efficiency set)⁶⁰, with a plane-wave cutoff of 110 Ry and a charge-density cutoff of 1320 Ry. Electronic smearing and partial occupancies were described with a Marzari-Vanderbilt-DeVita-Payne cold smearing⁶¹ with a spread of 0.01 Ry. In all periodic dimensions, the first Brillouin zone was sampled with a Γ -centered grid with a resolution of 0.125 \AA^{-1} .

C. Green-Kubo theory

The ionic conductivities, σ , are computed via the Green-Kubo theory of linear response^{62,63}, which is a practical framework for computing transport coefficients of extended systems^{64–67}. For an isotropic system of N interacting particles, it reads:

$$\sigma = \frac{\Omega}{3k_B T} \int_0^\infty \langle \mathbf{J}_q(\Gamma_t) \cdot \mathbf{J}_q(\Gamma_0) \rangle dt, \quad (1)$$

where Ω is the cell volume, k_B is the Boltzmann constant, T the temperature, and Γ_t indicates the time evolution of a point in phase space from the initial condition Γ_0 , over which the average $\langle \cdot \rangle$ is performed. \mathbf{J}_q is the charge flux, which depends only on the velocities of the atoms, \mathbf{v}_i , and their charges, q_i :

$$\mathbf{J}_q = \frac{e}{\Omega} \sum_i q_i \mathbf{v}_i. \quad (2)$$

Here, the sum runs over all the atoms, e is the electron charge, and the q_i are equal to the nominal oxidation numbers of the atoms.⁶⁸

D. Molecular dynamics and Monte Carlo simulations

$\text{Li}_3\text{YCl}_{6x}\text{Br}_{6(1-x)}$ has been reported in the $\bar{P}3m1$ and $C2/m$ phases, and in this work, we investigate the dependence of ionic conductivity on material composition for both phases in their fully ordered structure^{8,69}. The

conductivity, σ , is obtained from MD simulations using MLIPs developed in Sec. II B and implemented in LAMMPS^{70,71}. Two different simulation protocols are employed, depending on whether the system contains a single halide species (Li_3YBr_6 or Li_3YCl_6) or a mixed halide composition ($\text{Li}_3\text{YCl}_{6x}\text{Br}_{6(1-x)}$). For pure halide systems, we first perform a short 20 ps NpT equilibration run, followed by a 3 ns NpT production simulation from which the conductivity is extracted. For mixed compositions, we begin with a 20 ps equilibration in the NpT ensemble, followed by a 200 ps NpT simulation during which 100 Monte Carlo (MC) swaps between Br and Cl atoms are attempted every 100 fs. Fig. S3 in the SI shows the number of accepted swaps along trajectories of Li_3YClBr in the C2/m and P $\bar{3}$ m1 phases at different compositions, showing that the acceptance is around 12% for the whole simulations. In order to extract the conductivity, we select four snapshots spaced 50 ps apart from the NpT simulations with MC swaps; each snapshot is then equilibrated for 50 ps in the NpT ensemble, followed by a 3 ns production run for conductivity evaluation. All simulations were performed at ambient pressure and at a temperature of 300 K, consistent with the experimental conditions we use as reference.

III. RESULTS

A. Validation of the potential

We validate the bespoke potential trained for the SSEs on its test set, and compare the results with those from the universal potential. The zero-shot application of the PET-MAD already shows a good accuracy, in particular a RMSE of 17.34 meV/atom or energy and 86.29 meV/ \AA for forces, corresponding to an 8% of the force standard deviation in the test set. After the fine-tuning procedure, the error is reduced even further, with an RMSE of 1.38 meV/atom for energy and 39.16 meV/ \AA for forces, corresponding to 3.6% relative to the force standard deviation. Fig. S1 of the Supplementary Information contains the corresponding parity plots.

B. Phase stability

We assess the stability of the P $\bar{3}$ m1 and C2/m structures upon doping. To this end, we quenched the snapshots we obtained from MC sampling, optimizing their geometry using both PET-MAD and the fine-tuned potentials. Fig. 1 shows the formation energy, $\tilde{E}_{\text{Cl}_{6x}\text{Br}_{6(1-x)}}^\phi$, expressed relative to that of the C2/m polymorph as function of the alloying computed as follows:

$$\tilde{E}_{\text{Cl}_{6x}\text{Br}_{6(1-x)}}^\phi = E_{\text{Cl}_{6x}\text{Br}_{6(1-x)}}^\phi - \left[x E_{\text{Cl}_6}^{\text{C}2/\text{m}} + (1-x) E_{\text{Br}_6}^{\text{C}2/\text{m}} \right] \quad (3)$$

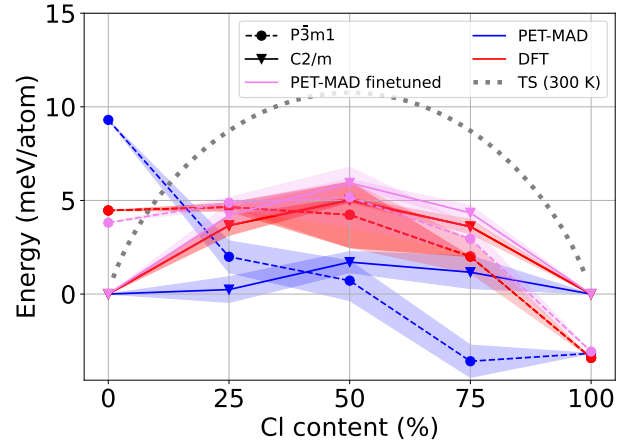


FIG. 1. Formation energy for the P $\bar{3}$ m1 and C2/m structures as a function of the Cl content, computed with both the PET-MAD potential and its fine-tuned version. For both potentials, the baseline energies are those of the C2/m phase. For the mixed composition, the results shown are the average values of the energies of the 4 structures selected from the MC, and the shaded areas represent the semi-dispersion of the results.

where $E_{\text{Cl}_{6x}\text{Br}_{6(1-x)}}^\phi$ is the energy of phase $\phi = \text{P}\bar{3}\text{m}1, \text{C}2/\text{m}$ and $x \in 0, 1$ is the concentration of Cl in the halide sites. To evaluate these energies, we used the final snapshots from the 3 ns NpT production runs, then we relaxed each structure by minimizing the atomic forces, and then computed the corresponding formation energies. For mixed compositions, the results shown in the figure are obtained by averaging the formation energies of the 4 snapshots extracted from the MC simulation, while the shaded area is the semi-dispersion of the four results.

As shown in Fig. 1, the different snapshots have energies that differ slightly, but the relative stability of the two phases follows clear trends, that are consistent between ML models and DFT reference. Both the zero-shot and fine-tuned models predict the C2/m phase to be more stable in the Br-rich part of the phase diagram, in agreement with experimental observations. The crossover is predicted to occur around 1:1 halide content, which is also consistent with experimental observations. PET-MAD predicts a small positive mixing enthalpy for the C2/m phase, and a small negative mixing enthalpy for the P $\bar{3}$ m1 phase. The fine-tuned model, instead, yields a positive mixing enthalpy for both phases. Comparison with single-point DFT calculations for the structure optimized with the fine-tuned model shows that – as expected – fine-tuning does improve the accuracy of the model. All sets of calculations are consistent with perfect miscibility at room temperature, as even in the case of the fine-tuned model, the positive mixing enthalpy is much smaller than the ideal solution entropy (that amounts to 10.8 meV/atom at 300 K for $x = 0.5$, see grey dotted line

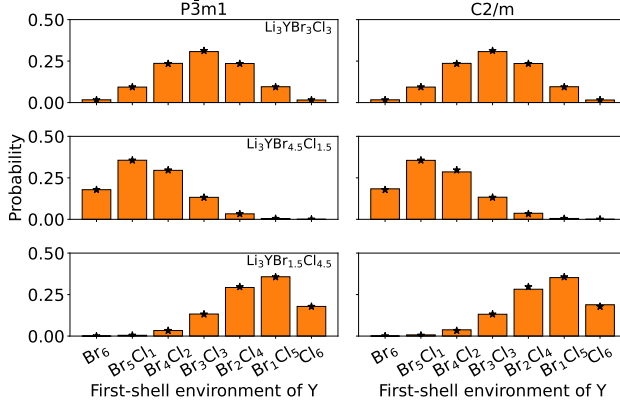


FIG. 2. Distribution of octahedral compositions in the first coordination shell of Y atoms during the MC simulation for the $P\bar{3}m1$ (first column) and $C2/m$ (second column) structures. Black stars indicate the expected values from a perfect binomial distribution, with p corresponding to the ratio between the number of Cl and the total number of halogen atoms in the formula units: 0.5 for the first row, 0.25 for the second, and 0.75 for the third. The heights of the bars and the distributions are normalized such that the total area sums to 1.

in Fig. 1). As we shall see below, this is consistent with an analysis of the finite-temperature MC/MD, which shows that the halides are randomly distributed in the alloy.

C. Structural effects of halide alloying

Experimental evidence shows that variations in the halide composition of SSEs affect their main structural features¹³. However, little is known about the spatial distribution of halogen atoms within these materials, specifically, whether they tend to cluster or remain randomly dispersed⁹. One way to assess the presence of short-range order in these alloys is to look at the composition of the octahedral units. In a random alloy, the number of Cl/Br anions in each octahedron should follow a binomial distribution depending on the overall composition, and any deviation would indicate the presence of correlations. We sample structures along the trajectories of the NpT simulations, where the MC swaps are attempted for both the $P\bar{3}m1$ (first column) and $C2/m$ (second column) structures, skipping the first 10 ps for equilibration. The results of Fig. 2 show perfect agreement between the histogram extracted from the simulations and the theoretical results, confirming that the distribution of the halides is random.

Another way to assess structural correlations is to analyze the radial distribution function (RDF). Figure 3 presents the partial RDFs for a system of $\text{Li}_3\text{YBr}_3\text{Cl}_3$ with the $P\bar{3}m1$ (left) and $C2/m$ (right) cell with both PET-MAD and the finetuned model. Snapshots were taken every 50 ps after an initial equilibration period of

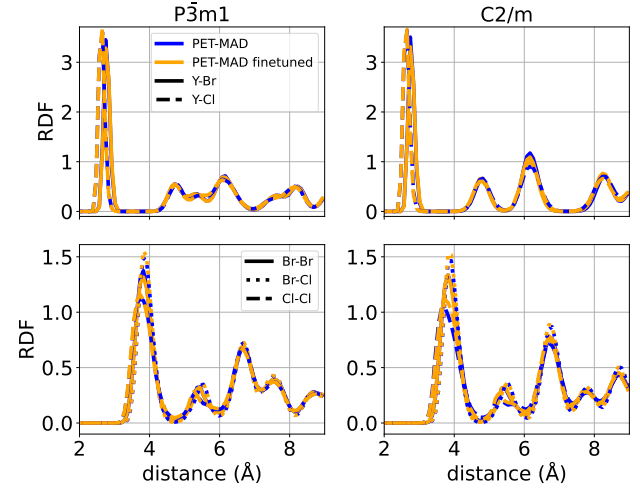


FIG. 3. Radial distribution functions (RDF) of a configuration of $\text{Li}_3\text{YBr}_3\text{Cl}_3$ in the $P\bar{3}m1$ phase (left) and $C2/m$ (right) for both the PET-MAD (blue) and the finetuned potential (orange). The upper panels contain the RDF between the Y atoms and the halogens: Y-Br (continuous), Y-Cl (dashed). The lower panels contain the RDF between the different halogen atoms: Br-Br (continuous), Br-Cl (dotted), Cl-Cl (dashed). These are extracted from the final 50 ps of 2 ns long NPT simulations.

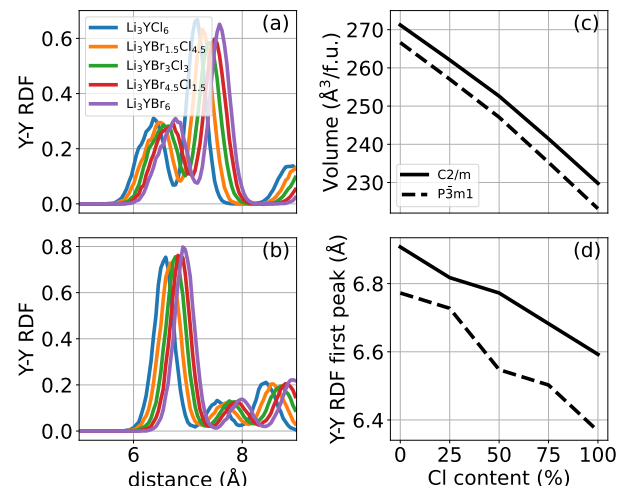


FIG. 4. Y-Y RDF for the $P\bar{3}m1$ (a), $C2/m$ (b) phases for the different chemical compositions. Behavior of the volume per formula unit (c) and the position of the first peak in the Y-Y RDF (b) as a function of the chemical composition.

100 ps. The partial RDFs show that the Y-Cl nearest-neighbor distance is slightly shorter than the Y-Br distance, but the long-range part of the RDFs is almost identical between different halide pairs, indicating that there is no medium-range order in the alloy. Even the comparison of the RDF of the 4 structures extracted from the MC simulations (see Fig. S4 in the Supple-

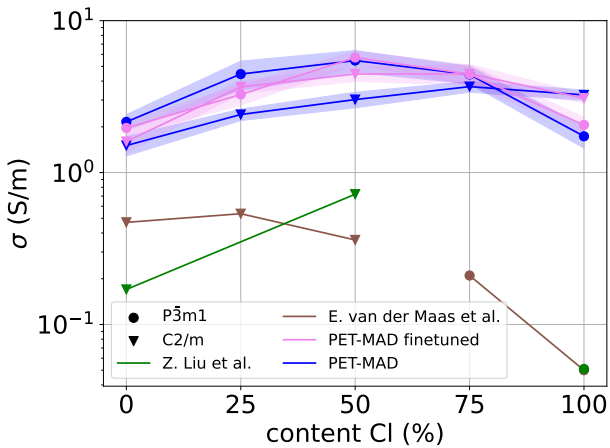


FIG. 5. Ionic conductivity (σ) of $\text{Li}_3\text{YBr}_{6(1-x)}\text{Cl}_{6x}$, with $x \in [0, 1]$, as a function of percentage of Cl content, computed via the PET-MAD universal potential (blue) and a PET model fine-tuned (pink line) on a specific dataset. The shaded area indicates the statistical uncertainty for the pure Li_3YBr_6 and Li_3YCl_6 phases; for the mixed composition, it indicates the semi-dispersion among the 4 from the different simulations selected during the MC procedure. Results are compared with experimental results reported in Refs.^{8,13} (green) and Ref.¹² (brown).

mentary information) reveals that all partial halide-halide RDFs exhibit similar behaviors. This indicates that Br and Cl atoms are randomly distributed with no preference for clustering at the level of individual YX_6 units, although differences in height of the first peak suggest a slight preference for Cl atoms being located at opposing corners of the octahedron. The zero-shot and fine-tuned models show almost perfect agreement, underscoring the high accuracy of the PET-MAD universal model.

The radial distribution functions can also help quantify the impact of alloying on the structural parameters. The bond length between the central metal atom in the octahedral site and the halogen atoms at its vertices remains nearly constant across different compositions. During molecular dynamics (MD) simulations, each structure relaxes to an average Y–Cl distance of 2.65 Å, and an average Y–Br distance of 2.74 Å. Conversely, the volume per formula unit decreases with increasing Cl content for both phases (see Fig. 4). This contraction is also reflected in the Y–Y RDF peaks, which show that a higher Cl concentration reduces Y–Y distances, increasing the packing of the octahedra.

D. Effects of alloying on the conductivity

We then move to consider the effect of alloying on the conductivity, performing simulations in the isothermal-isobaric ensemble, at ambient pressure and $T = 300$ K. Given that within the comparatively short time sampled

by our simulations both the $\text{P}\bar{3}\text{m}1$ and $\text{C}2/\text{m}$ phases are metastable across the full range of compositions, we perform simulations in both phases and at all concentrations. Fig. 5 shows the result of our simulations compared to the experimental results of Liu *et al.*¹³ and van der Maas *et al.*¹², that (as we discussed in the introduction) are not fully consistent with each other. In Fig. 5, the green points for Li_3YBr_6 and Li_3YCl_6 reported in Ref. 13 are the same conductivities obtained by Asano *et al.*⁸. The results obtained with the zero-shot PET-MAD universal potential (blue) and the fine-tuned model (pink) are in qualitative agreement with each other. The conductivity is overestimated by about 1 order of magnitude. The $\text{C}2/\text{m}$ phase shows a near-monotonic increase of σ with increasing Cl content, while the $\text{P}\bar{3}\text{m}1$ has a maximum around 1:1 alloying. Considering the experimental (and theoretical) stability, this is consistent with the observation by Liu *et al.*¹³ that the best performance can be achieved with $\approx 50\%$ doping. Despite the large overestimation of σ , our results predict an increase in σ also for the $\text{C}2/\text{m}$ phase, which corroborates the experimental observations in Ref. 13, and not those in Ref. 12, that show a decreasing conductivity upon doping of Li_3YBr with Cl.

Another important observation from Fig. 5 is the variability in conductivity arising from disorder in the halogen distribution. The conductivity of the four snapshots, taken from one another, can differ by as much as 20%. Given the small energy differences among the various halogen configurations shown in Fig. 1, it is likely that all of them can form under typical synthesis conditions, such as ball milling or hot pressing^{8,12,13,72}, resulting in real materials that represent an average of these configurations. In light of the qualitative discrepancy between experimental observations, and the large absolute shift in σ between measurements and theory, it is clear that the most important contribution that can come from our simulations is to reveal qualitative insights – e.g. they seem to support a maximum in σ around 1:1 alloy composition, in agreement with Liu *et al.*¹³. Given that in all our tests PET-MAD delivered qualitative behavior consistent with that of the fine-tuned model, we use the zero-shot universal model in the rest of our study, as it allows us to explore larger distortions and a wider portion of chemical space with no additional training cost.

E. Decoupling the volume and chemical composition dependence of the conductivity

The analysis performed in Section III C indicates that the main structural effect of alloying (besides modulating the stability of different phases) is to tune the metal-halide distance and the lattice parameters. To investigate the impact of these structural changes on the conductivity of the halide-based SSE, we conduct two computational experiments. To study the effects of the volume, we considered one of the 50% Cl 50% Br structures, and

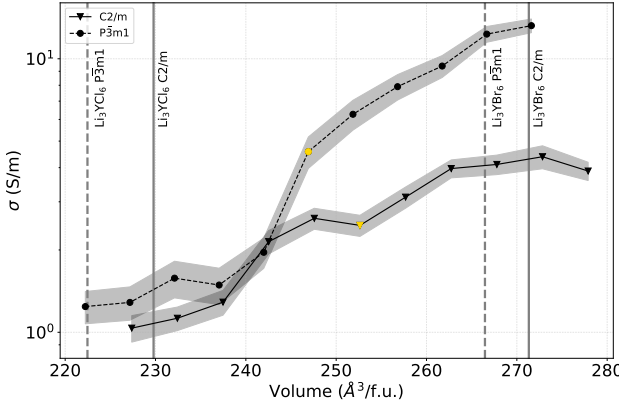


FIG. 6. Ionic conductivity as a function of volume for $\text{Li}_3\text{YBr}_3\text{Cl}_3$ in the C2/m (continuous line, triangle markers) and P3m1 (dashed line, circle markers) phases. Structures were selected from the MC simulation used in Fig. 5. For each phase, a representative snapshot with the average volume from the NPT simulation at 1 bar and 300 K was chosen. The volume was then varied by $\pm 10\%$, and the ionic conductivity was evaluated from NVT simulations at 300 K for each volume. Yellow markers indicate the relaxed cell at 1 bar and 300 K. The vertical lines represent the average volume per formula units, extracted from the NPT simulations, of the Li_3YBr_3 and Li_3YCl_3 for both phases.

modified the volume by $\pm 10\%$. For each volume, we performed a NVT thermalization simulation at 300K for 200 ps followed by a 3 ns NVT simulation to compute σ . Fig. 6 shows that the ionic conductivity is highly dependent on the volume for both structures, increasing the volume by around 5% increases σ by a factor of 2. The potential predicts that the P3m1 phase has a higher conductivity at almost all volumes. Given that increasing Cl concentration decreases the molar volume, this effect explains why Li_3YCl_6 has a sharp increase of σ upon alloying with Br.

We also perform the complementary experiment, studying the impact of the different chemical compositions on the conductivity independently from the volume effects. We fix the volume to that of the experimental structure in Ref.¹³ for the $\text{Li}_3\text{YCl}_3\text{Br}_3$ composition, then we sweep the different degrees of alloying, from full Br to full Cl substitution. Following the same procedure described in the previous section for the mixed composition: we performed a MC swap simulation in the NVT environment, from which 4 snapshots have been selected and then used to perform separate NVT simulations (one short equilibration of 50 ps followed by a production run of 3 ns). The maximum of the conductivity is achieved for a composition around 75% of Cl with an average conductivity that is around 8 times that obtained for the pure Br structure (Fig. 6).

In the Br-rich part of the composition space, the two effects compensate each other, explaining why the net effect observed in the NpT calculations (Fig. 4) is that of

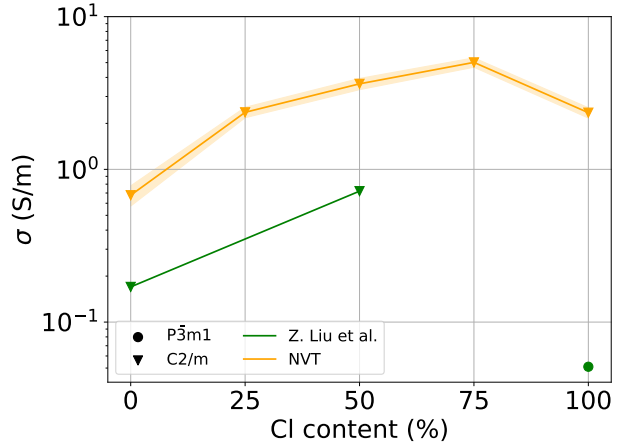


FIG. 7. Ionic conductivity as a function of the percentage Cl content. Every simulation in the yellow line is done at constant volume in the NVT ensemble at the volume of the $\text{Li}_3\text{YBr}_3\text{Cl}_3$ C2/m cell of Ref.^{8,13}.

increasing values of σ up to 50-75% Cl content, despite the reduction in molar volume that - alone - would reduce Li mobility. An interpretation of this compensation can be attempted based on the structural analysis in Section III C: (1) Increasing the Cl content also leads to a contraction of the octahedral framework (as evidenced by the Y-Y peak shift in Fig. 4), thereby reducing Li-ion mobility; (2) However, the presence of Cl, which forms shorter Y-Cl bonds, facilitates faster Li-ion migration. These insights provide valuable design principles for optimizing halide-based SSEs: achieving high conductivity requires balancing Cl concentration, which promotes Li diffusion, with maintaining a sufficiently large cell volume and stabilizing the P3m1 structure.

IV. INDIUM-YTTRIUM EXCHANGE

In the sections above, we have focused on the effects of halogen alloying on structure and conductivity. On the other hand, in solid-state electrolytes the use of metal alloying⁷³⁻⁷⁵ also proved to be an effective method to change the properties of the material. The use of a universal model, such as PET-MAD, that proved qualitatively accurate against a dedicated fine-tuned model, allows us to easily study the effect of alloying the metal ion. Li_3InCl_6 is a common halide SSE and is also found in the C2m structure⁷⁶. Starting from the structure in Sec. III D, we substitute the Y atoms with In and follow the same procedure presented in the previous sections to study the effects of halogen substitutions. Fig. 8 shows the behavior of $\text{Li}_3\text{InBr}_{6(1-x)}\text{Cl}_{6x}$ compared to the same behavior of $\text{Li}_3\text{YBr}_{6(1-x)}\text{Cl}_{6x}$ from Fig. 5, which is qualitatively very similar. The P3m1 structure has higher conductivity, and for 1:1 halogen doping, reaches the highest

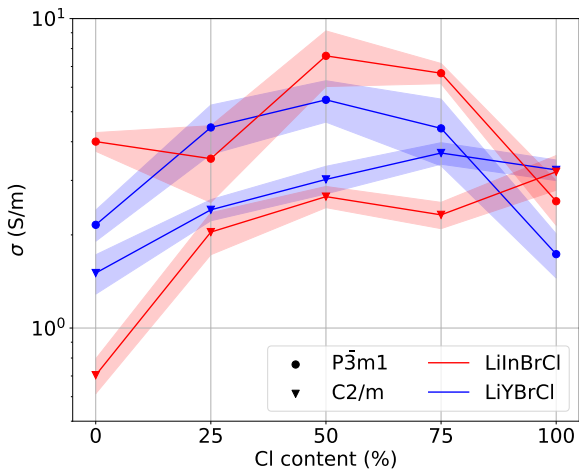


FIG. 8. Ionic conductivity of $\text{Li}_3\text{InBr}_{6(1-x)}\text{Cl}_{6x}$ (red) as a function of percentage of Cl content. Results are compared with those for $\text{Li}_3\text{YBr}_{6(1-x)}\text{Cl}_{6x}$ (blue) shown in Fig. 5. All conductivities are obtained from NPT simulations, following the procedure described in the main text, using the PET-MAD universal potential.

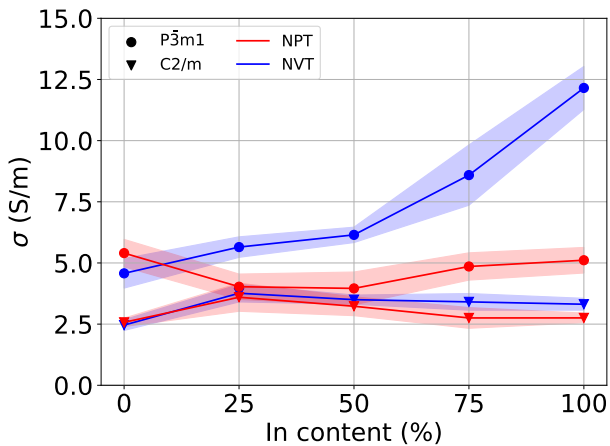


FIG. 9. Ionic conductivity (σ) of $\text{Li}_3\text{Y}_x\text{In}_{1-x}\text{Br}_3\text{Cl}_3$ as a function of percentage In content. Red points correspond to NPT simulations, and blue points to NVT simulations. For mixed compositions, the reported conductivity is the average over four distinct atomic configurations generated using the MC method described in the text. All simulations were performed using the PET-MAD universal potential.

value we observe. The C $\bar{2}$ /m phase has a lower conductivity, which increases almost monotonically in the Br \rightarrow Cl direction. As in the previous section our results can give important qualitative insights, even though they overestimate the conductivity of available experimental data, e.g. for Li_3InCl_6 σ is in the $[0.6 - 2.4] \times 10^{-1}$ S/m range depending on processing conditions.^{72,76-78}

We then compare constant-volume and constant-

pressure simulations for varying metal composition (Fig. 9). We fix the halide composition to a 1:1 ratio, select a single realization of the halide ordering and – for all intermediate Y-In compositions – perform an initial MC sampling of the metal ion positions and generate four initial configurations, that are used to perform independent trajectories to estimate σ . Note that this protocol means that Fig. 9 can show small inconsistencies with Fig. 8, that averages over four halide configurations. Especially for the P $\bar{3}$ m1 phase, there is a substantial interplay between volume and chemical effects, with a very large increase of conductivity with In content predicted at constant volume, but a much smaller variation observed when simulating at constant pressure. Overall, we find a small increase of σ for the C $\bar{2}$ /m phase, with a maximum at 25% In content, while the P $\bar{3}$ m1 phase shows high conductivity for pure $\text{Li}_3\text{InCl}_3\text{Br}_3$ and $\text{Li}_3\text{YCl}_3\text{Br}_3$, and lower conductivity at all intermediate concentrations.

V. CONCLUSIONS

This study demonstrates the enormous potential of generally-applicable machine-learning potentials for the study of complex functional materials, and provides some mechanistic insights into the interplay between structure and composition for halide-based solid-state electrolytes. The PET-MAD potential we use shows semi-quantitative agreement for both stability and charge transport in $\text{Li}_3\text{YCl}_{6x}\text{Br}_{6(1-x)}$ alloys with a more accurate model that is fine-tuned for this specific system. Both models indicate that the C $\bar{2}$ /m form is more stable for the Br-rich part of the phase diagram, with the P $\bar{3}$ m1 polymorph being more stable at high Cl concentrations, which is consistent with experimental observations. They also concur on predicting perfect miscibility of the two halides, and on the effectively random distribution of the ions, that show minimal indications of short-range ordering.

The conductivity is substantially overestimated compared with experiments, but once again the zero-shot model and the fine-tuned model are in qualitative agreement, finding an increase in σ with Cl content for the C $\bar{2}$ /m phase, and a maximum around the 1:1 composition for P $\bar{3}$ m1. These trends are consistent with Liu *et al.*⁷⁹, which suggests that the decreasing conductivity seen in van der Maas *et al.*¹² might be indicative of effects that go beyond bulk conductivity.

An important qualitative insight we can infer is how halide substitution modulates conductivity through the interplay of different effects. Besides controlling the stability of different polymorphs, substitution of Br with Cl leads to a decrease in volume of the structure, which in turns reduces σ . This effect is, however, compensated by the contraction of the YX_6 octahedra, which leaves more space for Li diffusion despite the contraction of the lattice. There is also significant variability in the values of σ depending on the sampling of the halide disorder, which makes it even more crucial to rely on MLIPs to be

able to simulate large supercells and to average several configurations.

A similar interplay between molar volume and local structure is seen when considering homovalent substitution of the metal ion. The trends of σ for $\text{Li}_3\text{InCl}_{6x}\text{Br}_{6(1-x)}$ are analogous to those seen in the Y compound, while the mixed In/Y compounds show large composition dependence of σ at constant volume, but much weaker variability when simulating at the equilibrium density for each composition. Although there is a significant quantitative discrepancy between simulations and experiments, which can likely be attributed to a combination of errors in the reference DFT method and limitations in estimating conductivity for an ideal crystalline bulk, our simulations suggest several design principles. First, the 1:1 halide composition seems to yield high values of σ across different polymorphs and metal compositions. Second, the molar volume and the metal-halide distances are important structural parameters that can be determined in the pure compounds and used as guides to test new alloys. Further exploration of the possible metals substitutions might provide additional insights, although the limited quantitative accuracy against the experimental conductivity makes it desirable to also investigate the use of better electronic-structure references, to facilitate predictive computational design of halide-

based solid-state electrolytes.

ACKNOWLEDGMENTS

We thank A. Mazitov and F. Bigi for helpful discussions about the use of PET-MAD and its fine-tuning strategies. DT thanks Manuel Dillenz for insightful comments on a first draft of the manuscript. DT and MC acknowledge support from a Sinergia grant of the Swiss National Science Foundation (grant ID CRSI5_2022296). MC acknowledges support from the European Research Council (ERC) under the research and innovation program (Grant Agreement No. 101001890-FIAMMA) and the NCCR MARVEL, funded by the Swiss National Science Foundation (SNSF, grant number 205602). This work was supported by grants from the Swiss National Supercomputing Centre (CSCS) under the projects s1243, s1219, lp26, and lp95.

DATA AVAILABILITY

All the data to reproduce the figures will be available on Material Cloud⁸⁰ upon publication.

* michele.ceriotti@epfl.ch

¹ Theodosios Famprikis, Pieremanuele Canepa, James A. Dawson, M. Saiful Islam, and Christian Masquelier, “Fundamentals of inorganic solid-state electrolytes for batteries,” *Nature Materials* **18**, 1278–1291 (2019).

² Jürgen Janek and Wolfgang G. Zeier, “A solid future for battery development,” *Nature Energy* **1**, 16141 (2016).

³ Jürgen Janek and Wolfgang G. Zeier, “Challenges in speeding up solid-state battery development,” *Nature Energy* (2023), 10.1038/s41560-023-01208-9.

⁴ Kyu-Nam Jung, Hyun-Seop Shin, Min-Sik Park, and Jong-Won Lee, “Solid-State Lithium Batteries: Bipolar Design, Fabrication, and Electrochemistry,” *ChemElectroChem* **6**, 3842–3859 (2019).

⁵ Changhong Wang, Jianwen Liang, Jung Tae Kim, and Xueliang Sun, “Prospects of halide-based all-solid-state batteries: From material design to practical application,” *Science Advances* **8**, eadc9516 (2022), <https://www.science.org/doi/pdf/10.1126/sciadv.adc9516>.

⁶ Se Young Kim, Kavish Kaup, Kern-Ho Park, Abdeljalil Assoud, Laidong Zhou, Jue Liu, Xiaohan Wu, and Linda F. Nazar, “Lithium ytterbium-based halide solid electrolytes for high voltage all-solid-state batteries,” *ACS Materials Letters* **3**, 930–938 (2021).

⁷ Hiram Kwak, Daseul Han, Jeyne Lyoo, Juhyoun Park, Sung Hoo Jung, Yoonjae Han, Gihan Kwon, Hansu Kim, Seung-Tae Hong, Kyung-Wan Nam, and Yoon Seok Jung, “New cost-effective halide solid electrolytes for all-solid-state batteries: Mechanochemically prepared Fe^{3+} -substituted Li_2ZrCl_6 ,” *Advanced Energy Materials* **11**, 2003190 (2021).

⁸ Tetsuya Asano, Akihiro Sakai, Satoru Ouchi, Masashi Sakaida, Akinobu Miyazaki, and Shinya Hasegawa, “Solid Halide Electrolytes with High Lithium-Ion Conductivity for Application in 4 V Class Bulk-Type All-Solid-State Batteries,” *Advanced Materials* **30**, 1–7 (2018).

⁹ Qingtao Wang, Zhenyang Shen, Pengfei Du, Yongmei Zhou, Peng Zhang, and Ying Liu, “New advances in solid-state electrolytes: from halides to oxyhalides,” *Inorg. Chem. Front.* **11**, 5810–5832 (2024).

¹⁰ Ruishan Zhang, Shunning Li, Feng Pan, and Bingkai Zhang, “High ionic conductivity and cost-effective halide solid electrolyte enabled by long-range cooperative transport in bi-doped Li_2ZrCl_6 ,” *Chemistry of Materials* (2025), 10.1021/acs.chemmater.5c01711.

¹¹ Zhu Cheng, Wexuan Zhao, Qidi Wang, Chenglong Zhao, Anastasia K. Lavrinenko, Alexandros Vasileiadis, Victor Landgraf, Lars Bannenberg, Yuhang Li, Junwei Liang, Ming Liu, Swapna Ganapathy, and Marnix Wagemaker, “Beneficial redox activity of halide solid electrolytes empowering high-performance anodes in all-solid-state batteries,” *Nature Materials* (2025).

¹² Eveline van der Maas, Wexuan Zhao, Zhu Cheng, Theodosios Famprikis, Michel Thijs, Steven R. Parnell, Swapna Ganapathy, and Marnix Wagemaker, “Investigation of structure, ionic conductivity, and electrochemical stability of halogen substitution in solid-state ion conductor $\text{Li}_3\text{YBr}_x\text{Cl}_{6-x}$,” *The Journal of Physical Chemistry C* **127**, 125–132 (2023).

¹³ Zhantao Liu, Shuan Ma, Jue Liu, Shan Xiong, Yifan Ma, and Hailong Chen, “High Ionic Conductivity Achieved in $\text{Li}_3\text{Y}(\text{Br}_3\text{Cl}_3)$ Mixed Halide Solid Electrolyte via Pro-

- moted Diffusion Pathways and Enhanced Grain Boundary,” ACS Energy Letters **6**, 298–304 (2021).
- ¹⁴ Weijian Chen, Yumeng Zhao, Jiahe Zhou, Shuting Li, Chuanyang Lu, Shoubin Zhou, Huixin Li, Yafei Li, Yuwen Cheng, Jianguo Yang, Yanming He, and Jiayan Luo, “High-throughput screening of halide solid-state electrolytes for all-solid-state li-ion batteries through structural descriptor,” Journal of Alloys and Compounds **1010**, 177167 (2025).
- ¹⁵ Rui Li, Kaiqi Xu, Kaining Liu, Rui Si, and Zhizhen Zhang, “Computational Screening of Na₃ MBr₆ Compounds as Sodium Solid Electrolytes,” Chemistry of Materials **34**, 8356–8365 (2022).
- ¹⁶ Ballal Ahammed and Elif Ertekin, “Configurational disorder, strong anharmonicity, and coupled host dynamics lead to superionic transport in Li₃Cycl (lyc),” Advanced Materials **36**, 2310537 (2024), <https://advanced.onlinelibrary.wiley.com/doi/pdf/10.1002/adma.202310537>
- ¹⁷ Nongnuch Artrith, “Machine learning for the modeling of interfaces in energy storage and conversion materials,” Journal of Physics: Energy **1**, 032002 (2019).
- ¹⁸ Zhizhen Zhang, Hui Li, Kavish Kaup, Laidong Zhou, Pierre-Nicholas Roy, and Linda F. Nazar, “Targeting Superionic Conductivity by Turning on Anion Rotation at Room Temperature in Fast Ion Conductors,” Matter **2**, 1667–1684 (2020).
- ¹⁹ Jeffrey G. Smith and Donald J. Siegel, “Low-temperature paddlewheel effect in glassy solid electrolytes,” Nature Communications **11**, 1483 (2020).
- ²⁰ N. D. Lepley, N. A. W. Holzwarth, and Yaojun A. Du, “Structures, Li + mobilities, and interfacial properties of solid electrolytes Li₃PS₄ and Li₃PO₄ from first principles,” Phys. Rev. B **88**, 104103 (2013).
- ²¹ Volker L. Deringer, Albert P. Bartók, Noam Bernstein, David M. Wilkins, Michele Ceriotti, and Gábor Csányi, “Gaussian process regression for materials and molecules,” Chemical Reviews **121**, 10073–10141 (2021).
- ²² Han Wang, Linfeng Zhang, Jiequn Han, and Weinan E, “DeepMD-kit: A deep learning package for many-body potential energy representation and molecular dynamics,” Computer Physics Communications **228**, 178–184 (2018).
- ²³ Jinzhe Zeng, Duo Zhang, Denghui Lu, Pinghui Mo, Zeyu Li, Yixiao Chen, Marián Ryník, Li’ang Huang, Ziyao Li, Shaochen Shi, Yingze Wang, Haotian Ye, Ping Tuo, Jiabin Yang, Ye Ding, Yifan Li, Davide Tisi, Qiyu Zeng, Han Bao, Yu Xia, Jiameng Huang, Koki Muraoka, Yibo Wang, Junhan Chang, Fengbo Yuan, Sigríður Þórhalla Bore, Chun Cai, Yinnian Lin, Bo Wang, Jiayan Xu, Jia-Xin Zhu, Chenxing Luo, Yuzhi Zhang, Rhys E. A. Goodall, Wenshuo Liang, Anurag Kumar Singh, Sikai Yao, Jingchao Zhang, Renata Wentzcovitch, Jiequn Han, Jie Liu, Weile Jia, Darren M. York, Weinan E, Roberto Car, Linfeng Zhang, and Han Wang, “DeePMD-kit v2: A software package for deep potential models,” The Journal of Chemical Physics **159**, 054801 (2023).
- ²⁴ Albert P. Bartók, Mike C Payne, Risi Kondor, and Gábor Csányi, “Gaussian Approximation Potentials: The Accuracy of Quantum Mechanics, without the Electrons,” Physical Review Letters **104**, 136403 (2010).
- ²⁵ J. Behler and M. Parrinello, “Generalized Neural-Network Representation of High-Dimensional Potential-Energy Surfaces,” Physical Review Letters **98**, 146401 (2007).
- ²⁶ J. S. Smith, O. Isayev, and A. E. Roitberg, “ANI-1: an extensible neural network potential with DFT accuracy at force field computational cost,” Chemical Science **8**, 3192–3203 (2017).
- ²⁷ Kristof T. Schütt, Stefaan S. P. Hessmann, Niklas W. A. Gebauer, Jonas Lederer, and Michael Gastegger, “SchNet-Pack 2.0: A neural network toolbox for atomistic machine learning,” The Journal of Chemical Physics **158**, 144801 (2023).
- ²⁸ Matthias Rupp, Alexandre Tkatchenko, Klaus-Robert Müller, and O. Anatole von Lilienfeld, “Fast and Accurate Modeling of Molecular Atomization Energies with Machine Learning,” Physical Review Letters **108**, 058301 (2012), 1109.2618.
- ²⁹ Keith T. Butler, Daniel W. Davies, Hugh Cartwright, Olexandr Isayev, and Aron Walsh, “Machine learning for molecular and materials science,” Nature **559**, 547–555 (2018).
- ³⁰ Tsz Wai Ko, Jonas A. Finkler, Stefan Goedecker, and Jörg ^{29234053A} fourth-generation high-dimensional neural network potential with accurate electrostatics including non-local charge transfer,” Nature Communications **12**, 398 (2021).
- ³¹ Oliver T. Unke and Markus Meuwly, “Physnet: A neural network for predicting energies, forces, dipole moments, and partial charges,” Journal of Chemical Theory and Computation **15**, 3678–3693 (2019).
- ³² Simon Batzner, Albert Musaelian, Lixin Sun, Mario Geiger, Jonathan P. Mailoa, Mordechai Kornbluth, Nicola Molinari, Tess E. Smidt, and Boris Kozinsky, “E(3)-equivariant graph neural networks for data-efficient and accurate interatomic potentials,” Nat. Commun. **13**, 2453 (2022).
- ³³ Zheyong Fan, Zezhu Zeng, Cunzhi Zhang, Yanzhou Wang, Keke Song, Haikuan Dong, Yue Chen, and Tapio Ala-Nissila, “Neuroevolution machine learning potentials: Combining high accuracy and low cost in atomistic simulations and application to heat transport,” Phys. Rev. B **104**, 104309 (2021).
- ³⁴ Takeru Miyagawa, Namita Krishnan, Manuel Grumet, Christian Reverón Baecker, Waldemar Kaiser, and David A. Egger, “Accurate description of ion migration in solid-state ion conductors from machine-learning molecular dynamics,” Journal of Materials Chemistry A **12**, 11344–11361 (2024).
- ³⁵ Davide Tisi, Federico Grasselli, Lorenzo Gigli, and Michele Ceriotti, “Thermal conductivity of Li₃PS₄ solid electrolytes with *ab initio* accuracy,” Phys. Rev. Materials **8**, 065403 (2024).
- ³⁶ Carsten G. Staacke, Tabea Huss, Johannes T. Margraf, Karsten Reuter, and Christoph Scheurer, “Tackling structural complexity in Li₂S-P₂S₅ solid-state electrolytes using machine learning potentials,” Nanomaterials **12**, 2950 (2022).
- ³⁷ Lorenzo Gigli, Davide Tisi, Federico Grasselli, and Michele Ceriotti, “Mechanism of Charge Transport in Lithium Thiophosphate,” Chem. Mater. **36**, 1482–1496 (2024).
- ³⁸ Xingyu Guo, Zhenbin Wang, Ji-Hui Yang, and Xin-Gao Gong, “Machine-learning assisted high-throughput discovery of solid-state electrolytes for li-ion batteries,” J. Mater. Chem. A **12**, 10124–10136 (2024).
- ³⁹ Paolo Pegolo, Stefano Baroni, and Federico Grasselli, “Temperature-and vacancy-concentration-dependence of heat transport in Li₃ClO from multi-method numerical simulations,” npj Comput. Mater. **8**, 24 (2022).

- ⁴⁰ Austin D. Sendek, Brandi Ransom, Ekin D. Cubuk, Lenson A. Pellochoud, Jagjit Nanda, and Evan J. Reed, “Machine Learning Modeling for Accelerated Battery Materials Design in the Small Data Regime,” *Advanced Energy Materials* **12**, 2200553 (2022).
- ⁴¹ Hanna Türk, Davide Tisi, and Michele Ceriotti, “Reconstructions and dynamics of β -lithium thiophosphate surfaces,” *PRX Energy* **4**, 033010 (2025).
- ⁴² Min Lin, Jingfang Xiong, Mintao Su, Feng Wang, Xiangsi Liu, Yifan Hou, Riqiang Fu, Yong Yang, and Jun Cheng, “A machine learning protocol for revealing ion transport mechanisms from dynamic nmr shifts in paramagnetic battery materials,” *Chem. Sci.* **13**, 7863–7872 (2022).
- ⁴³ Artem D. Dembitskiy, Innokenti S. Humonen, Roman A. Eremin, Dmitry A. Aksyonov, Stanislav S. Fedotov, and Semen A. Budennyy, “Benchmarking machine learning models for predicting lithium ion migration,” *npj Computational Materials* **11**, 131 (2025).
- ⁴⁴ Ilyes Batatia, Philipp Benner, Yuan Chiang, Alin M Elena, Dávid P Kovács, Janosh Riebesell, Xavier R Advincula, Mark Asta, Matthew Avaylon, William J Baldwin, *et al.*, “A foundation model for atomistic materials chemistry,” arXiv preprint arXiv:2401.00096 (2023).
- ⁴⁵ Han Yang, Chenxi Hu, Yichi Zhou, Xixian Liu, Yu Shi, Jielan Li, Guanzhi Li, Zekun Chen, Shuizhou Chen, Claudio Zeni, *et al.*, “Mattersim: A deep learning atomistic model across elements, temperatures and pressures,” arXiv preprint arXiv:2405.04967 (2024).
- ⁴⁶ Mark Neumann, James Gin, Benjamin Rhodes, Steven Bennett, Zhiyi Li, Hitarth Choubisa, Arthur Hussey, and Jonathan Godwin, “Orb: A fast, scalable neural network potential,” (2024), arXiv:2410.22570 [cond-mat.mtrl-sci].
- ⁴⁷ Arslan Mazitov, Filippo Bigi, Matthias Kellner, Paolo Peggio, Davide Tisi, Guillaume Fraux, Sergey Pozdnyakov, Philip Loche, and Michele Ceriotti, “Pet-mad, a universal interatomic potential for advanced materials modeling,” (2025), arXiv:2503.14118 [cond-mat.mtrl-sci].
- ⁴⁸ Arslan Mazitov, Sofia Chorna, Guillaume Fraux, Marnik Bercx, Giovanni Pizzi, Sandip De, and Michele Ceriotti, “Massive atomic diversity: a compact universal dataset for atomistic machine learning,” (2025), arXiv:2506.19674 [cond-mat.mtrl-sci].
- ⁴⁹ Sergey Pozdnyakov and Michele Ceriotti, “Smooth, exact rotational symmetrization for deep learning on point clouds,” in *Advances in Neural Information Processing Systems*, Vol. 36, edited by A. Oh, T. Naumann, A. Globerson, K. Saenko, M. Hardt, and S. Levine (Curran Associates, Inc., 2023) pp. 79469–79501.
- ⁵⁰ Ashish Vaswani, Noam Shazeer, Niki Parmar, Jakob Uszkoreit, Llion Jones, Aidan N Gomez, Łukasz Kaiser, and Illia Polosukhin, “Attention is all you need,” *Advances in neural information processing systems* **30** (2017).
- ⁵¹ Leon Bergen, Timothy J. O’Donnell, and Dzmitry Bahdanau, “Systematic generalization with edge transformers,” in *Proceedings of the 35th International Conference on Neural Information Processing Systems*, NIPS ’21 (Curran Associates Inc., Red Hook, NY, USA, 2021).
- ⁵² Simon Batzner, Albert Musaelian, Lixin Sun, Mario Geiger, Jonathan P Mailoa, Mordechai Kornbluth, Nicola Molinari, Tess E Smidt, and Boris Kozinsky, “ $E(3)$ -equivariant graph neural networks for data-efficient and accurate interatomic potentials,” *Nature communications* **13**, 2453 (2022).
- ⁵³ Albert Musaelian, Simon Batzner, Anders Johansson, Lixin Sun, Cameron J. Owen, Mordechai Kornbluth, and Boris Kozinsky, “Learning local equivariant representations for large-scale atomistic dynamics,” (2022), arXiv:2204.05249 [physics.comp-ph].
- ⁵⁴ Marcel F Langer, Sergey N Pozdnyakov, and Michele Ceriotti, “Probing the effects of broken symmetries in machine learning,” *Machine Learning: Science and Technology* **5**, 04LT01 (2024).
- ⁵⁵ Paolo Giannozzi, Stefano Baroni, Nicola Bonini, Matteo Calandra, Roberto Car, Carlo Cavazzoni, Davide Ceresoli, Guido L Chiarotti, Matteo Cococcioni, Ismaila Dabo, Andrea Dal Corso, Stefano de Gironcoli, Stefano Fabris, Guido Fratesi, Ralph Gebauer, Uwe Gerstmann, Christos Gougaussis, Anton Kokalj, Michele Lazzeri, Layla Martin-Samos, Nicola Marzari, Francesco Mauri, Riccardo Mazzarello, Stefano Paolini, Alfredo Pasquarello, Lorenzo Paulatto, Carlo Sbraccia, Sandro Scandolo, Gabriele Sclauzero, Ari P Seitsonen, Alexander Smogunov, Paolo Umari, and Renata M Wentzcovitch, “QUANTUM ESPRESSO: a modular and open-source software project for quantum simulations of materials,” *J. Phys. Cond. Matt.* **21**, 395502–395519 (2009).
- ⁵⁶ P. Giannozzi, O. Andreussi, T. Brumme, O. Bunau, M. Buongiorno Nardelli, M. Calandra, R. Car, C. Cavazzoni, D. Ceresoli, M. Cococcioni, N. Colonna, I. Carnimeo, A. Dal Corso, S. de Gironcoli, P. Delugas, R. A. DiStasio, A. Ferretti, A. Floris, G. Fratesi, G. Fugallo, R. Gebauer, U. Gerstmann, F. Giustino, T. Gorni, J. Jia, M. Kawamura, H.-Y. Ko, A. Kokalj, E. Küçükbenli, M. Lazzeri, M. Marsili, N. Marzari, F. Mauri, N. L. Nguyen, H.-V. Nguyen, A. Otero-de-la Roza, L. Paulatto, S. Poncé, D. Rocca, R. Sabatini, B. Santra, M. Schlipf, A. P. Seitsonen, A. Smogunov, I. Timrov, T. Thonhauser, P. Umari, N. Vast, X. Wu, and S. Baroni, “Advanced capabilities for materials modelling with Quantum ESPRESSO,” *Journal of Physics: Condensed Matter* **29**, 465901 (2017).
- ⁵⁷ Paolo Giannozzi, Oscar Baseggio, Pietro Bonfà, Davide Brunato, Roberto Car, Ivan Carnimeo, Carlo Cavazzoni, Stefano de Gironcoli, Pietro Delugas, Fabrizio Ferrari Ruffino, Andrea Ferretti, Nicola Marzari, Iurii Timrov, Andrea Urru, and Stefano Baroni, “Quantum ESPRESSO toward the exascale,” *The Journal of Chemical Physics* **152**, 154105 (2020).
- ⁵⁸ Ivan Carnimeo, Fabio Affinito, Stefano Baroni, Oscar Baseggio, Laura Bellentani, Riccardo Bertossa, Pietro Davide Delugas, Fabrizio Ferrari Ruffino, Sergio Orlandini, Filippo Spiga, and Paolo Giannozzi, “Quantum espresso: One further step toward the exascale,” *Journal of Chemical Theory and Computation* **19**, 6992–7006 (2023).
- ⁵⁹ John P. Perdew, Adrienn Ruzsinszky, Gábor I. Csonka, Oleg A. Vydrov, Gustavo E. Scuseria, Lucian A. Constantin, Xiaolan Zhou, and Kieron Burke, “Restoring the density-gradient expansion for exchange in solids and surfaces,” *Phys. Rev. Lett.* **100**, 136406 (2008).
- ⁶⁰ Gianluca Prandini, Antimo Marrazzo, Ivano E. Castelli, Nicolas Mounet, and Nicola Marzari, “Precision and efficiency in solid-state pseudopotential calculations,” *npj Comput Mater* **4**, 72 (2018).
- ⁶¹ Nicola Marzari, David Vanderbilt, Alessandro De Vita, and M. C. Payne, “Thermal Contraction and Disordering of the Al(110) Surface,” *Phys. Rev. Lett.* **82**, 3296–3299 (1999).

- ⁶² M. S. Green, "Markoff random processes and the statistical mechanics of time-dependent phenomena, II. Irreversible processes in fluids," *J. Chem. Phys.* **22**, 398 – 413 (1954).
- ⁶³ R. Kubo, "Statistical-mechanical theory of irreversible processes. I. General Theory and Simple Applications to Magnetic and Conduction Problems," *J. Phys. Soc. Jpn.* **12**, 570 – 586 (1957).
- ⁶⁴ Lorenzo Gigli, Davide Tisi, Federico Grasselli, and Michele Ceriotti, "Mechanism of charge transport in lithium thiophosphate," *Chemistry of Materials* **36**, 1482–1496 (2024), <https://doi.org/10.1021/acs.chemmater.3c02726>.
- ⁶⁵ Davide Tisi, Linfeng Zhang, Riccardo Bertossa, Han Wang, Roberto Car, and Stefano Baroni, "Heat transport in liquid water from first-principles and deep neural network simulations," *Phys. Rev. B* **104**, 224202 (2021).
- ⁶⁶ Davide Tisi, Federico Grasselli, Lorenzo Gigli, and Michele Ceriotti, "Thermal conductivity of Li_3PS_4 solid electrolytes with ab initio accuracy," *Phys. Rev. Mater.* **8**, 065403 (2024).
- ⁶⁷ Cesare Malosso, Linfeng Zhang, Roberto Car, Stefano Baroni, and Davide Tisi, "Viscosity in water from first-principles and deep-neural-network simulations," *npj Computational Materials* **8**, 139 (2022).
- ⁶⁸ Federico Grasselli and Stefano Baroni, "Topological quantization and gauge invariance of charge transport in liquid insulators," *Nature Physics* **15**, 967–972 (2019).
- ⁶⁹ Roman Schlem, Sokseoha Muy, Nils Prinz, Ananya Banik, Yang Shao-Horn, Mirijam Zobel, and Wolfgang G. Zeier, "Mechanochemical synthesis: A tool to tune cation site disorder and ionic transport properties of Li_3MCl_6 ($\text{m} = \text{y}, \text{er}$) superionic conductors," *Advanced Energy Materials* **10**, 1903719 (2020).
- ⁷⁰ Steve Plimpton, "Fast Parallel Algorithms for Short-Range Molecular Dynamics," *J. Comp. Phys.* **117**, 1–19 (1995).
- ⁷¹ A. P. Thompson, H. M. Aktulga, R. Berger, D. S. Bolittleanu, W. M. Brown, P. S. Crozier, P. J. in 't Veld, A. Kohlmeyer, S. G. Moore, T. D. Nguyen, R. Shan, M. J. Stevens, J. Tranchida, C. Trott, and S. J. Plimpton, "LAMMPS - a flexible simulation tool for particle-based materials modeling at the atomic, meso, and continuum scales," *Comp. Phys. Comm.* **271**, 108171 (2022).
- ⁷² Xiaona Li, Jianwen Liang, Jing Luo, Mohammad Norouzi Banis, Changhong Wang, Weihan Li, Sixu Deng, Chuang Yu, Feipeng Zhao, Yongfeng Hu, Tsun-Kong Sham, Li Zhang, Shangqian Zhao, Shigang Lu, Huan Huang, Ruying Li, Keegan R. Adair, and Xueliang Sun, "Air-stable Li_3InCl_6 electrolyte with high voltage compatibility for all-solid-state batteries," *Energy Environ. Sci.* **12**, 2665–2671 (2019).
- ⁷³ Chao Wu, Zhen Wang, Zhanhui Jia, Jiawu Cui, Chengyong Shu, Xiaowei Wang, Yuping Wu, and Wei Tang, "Insights into chemical substitution of metal halide solid-state electrolytes for all-solid-state lithium batteries," *EES Batteries* **1**, 364–384 (2025).
- ⁷⁴ Xu Han, Yang Xu, Huamei Li, Zaifa Wang, Junyi Yue, Xiaolong Yan, Simeng Zhang, Jiamin Fu, Yu Xia, Liyu Zhou, Saiqi Wei, Xinyi Liu, Xingyu Wang, Changtai Zhao, Xiaona Li, Shou-Hang Bo, Jiantao Wang, Xueliang Sun, and Jianwen Liang, "Mechanically robust halide electrolytes for high-performance all-solid-state batteries," *Nature Communications* **16**, 9770 (2025).
- ⁷⁵ Farzaneh Bahmani and Alevtina White Smirnova, "Dual substitution in cationic and anionic sublattices of lithium indium chloride for high-performance solid-state lithium metal batteries," *J. Mater. Chem. A* **13**, 18732–18742 (2025).
- ⁷⁶ Rundi Xiong, Lixia Yuan, Ruifeng Song, Shuaipeng Hao, Haijin Ji, Zexiao Cheng, Yi Zhang, Bowen Jiang, Yudi Shao, Zhen Li, and Yunhui Huang, "Solvent-Mediated Synthesis and Characterization of Li_3InCl_6 Electrolytes for All-Solid-State Li-Ion Battery Applications," *ACS Applied Materials & Interfaces* **16**, 36281–36288 (2024).
- ⁷⁷ C. Rosa, A. Pesce, P. Lannelongue, M. Ravalli, J.M. López del Amo, P. López-Aranguren, E. Quartarone, and C. Tealdi, "Understanding interfacial stability and ionic transport in ethanol-synthesized Li_3InCl_6 solid electrolyte for all-solid-state batteries," *Journal of Physics and Chemistry of Solids* **209**, 113327 (2026).
- ⁷⁸ Xiaona Li, Jianwen Liang, Ning Chen, Jing Luo, Keegan R. Adair, Changhong Wang, Mohammad Norouzi Banis, Tsun-Kong Sham, Li Zhang, Shangqian Zhao, Shigang Lu, Huan Huang, Ruying Li, and Xueliang Sun, "Water-Mediated Synthesis of a Superionic Halide Solid Electrolyte," *Angewandte Chemie* **131**, 16579–16584 (2019).
- ⁷⁹ Zengcai Liu, Wujun Fu, E. Andrew Payzant, Xiang Yu, Zili Wu, Nancy J. Dudney, Jim Kiggans, Kunlun Hong, Adam J. Rondinone, and Chengdu Liang, "Anomalous high ionic conductivity of nanoporous $\beta\text{-Li}_3\text{PS}_4$," *Journal of the American Chemical Society* **135**, 975–978 (2013).
- ⁸⁰ Leopold Talirz, Snehal Kumbhar, Elsa Passaro, Aliaksandr V. Yakutovich, Valeria Granata, Fernando Gargiulo, Marco Borelli, Martin Uhrin, Sebastiaan P. Huber, Spyros Zoupanos, Carl S. Adorf, Casper Welzel Andersen, Ole Schütt, Carlo A. Pignedoli, Daniele Passerone, Joost Vandevondele, Thomas C. Schultheiss, Berend Smit, Giovanni Pizzi, and Nicola Marzari, "Materials cloud, a platform for open computational science," *Scientific Data* **7**, 299 (2020).

Supplementary Informations of Mechanistic study of mixed lithium halides solid state electrolytes

Davide Tisi,¹ Sergey Pozdnyakov,¹ and Michele Ceriotti^{1,*}

¹*Laboratory of Computational Science and Modeling, Institut des Matériaux,
École Polytechnique Fédérale de Lausanne, 1015 Lausanne, Switzerland*

(Dated: November 14, 2025)

* michele.ceriotti@epfl.ch

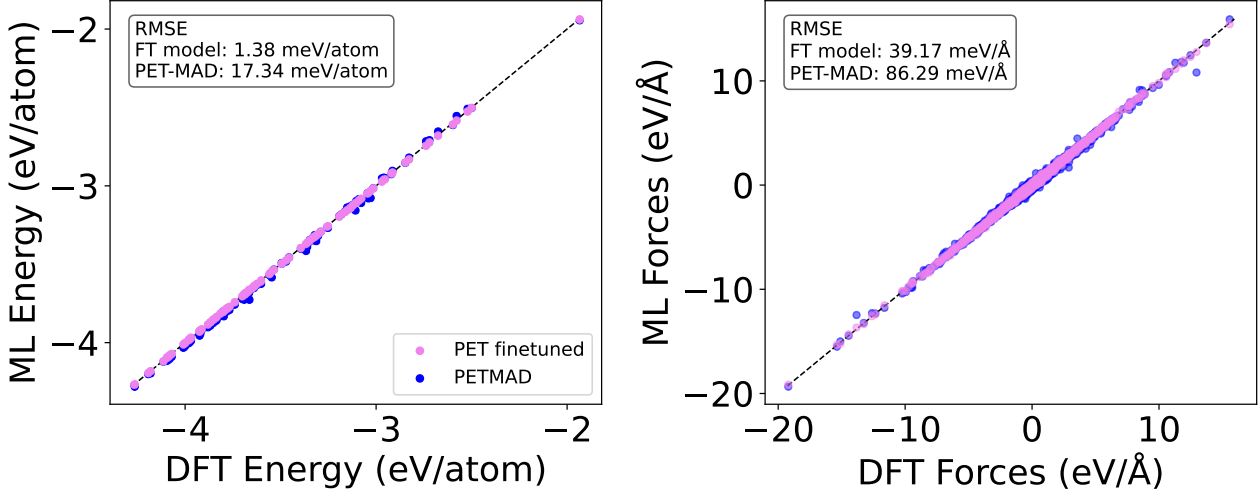


FIG. S1. Parity plot of the energy (left panel) and atomic forces (right panel) for the PET-MAD universal potential and PET-fine-tuned model.

I. PARITY PLOT

Fig. S1 shows the parity plot for energy and forces of the PET-MAD universal potential (blue) and the finetuned model (violet) computed for a test set. The figure also shows the root-mean-square-errors (RMSE) for both energies and forces of both models. The RMSE is computed using these definitions:

$$RMSE_E = \sqrt{\frac{\sum_t (E_t^{ML} - E_t^{DFT})^2}{N_{set}}} \quad (S1)$$

$$RMSE_F = \sqrt{\frac{\sum_t \sum_j \sum_{\alpha \in x,y,z} (F_{tj\alpha}^{ML} - F_{tj\alpha}^{DFT})^2}{3N_{atoms}}} \quad (S2)$$

where E_t^{ML} and E_t^{DFT} are the energy of snapshot t predicted by the ML model and by the DFT reference, respectively. The sum of t runs over all the N_{set} snapshots in the test set. $F_{tj\alpha}^{ML}$ and $F_{tj\alpha}^{DFT}$ represent the prediction of the α component of the force acting on atom j in the snapshot t . N_{atoms} represents the total number of atoms in all the structures in the test set.

II. SIZE SCALING

Fig. S2 shows conductivity as a function of the size of the system for the system of pure Br and Cl in both crystal structures. The vertical dashed lines represent the size of 960 atoms, used in the main results of this work. At that size the result is completely converged.

III. MC STABILITY

Fig. S3 shows the evolution of the acceptance rate of Monte Carlo (MC) swaps during the simulation of $\text{LiYBr}_{6(1-x)}\text{Cl}_{6x}$ in the both phases at all the different compositions. After an initial thermalization period, the system reaches a stable number of accepted swaps, indicating equilibration. On average 12% of swaps-per-step are accepted.

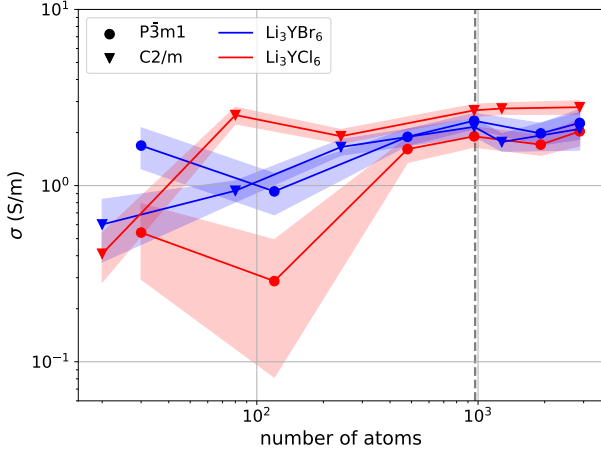


FIG. S2. Size scaling of the conductivity for different structures and lattice

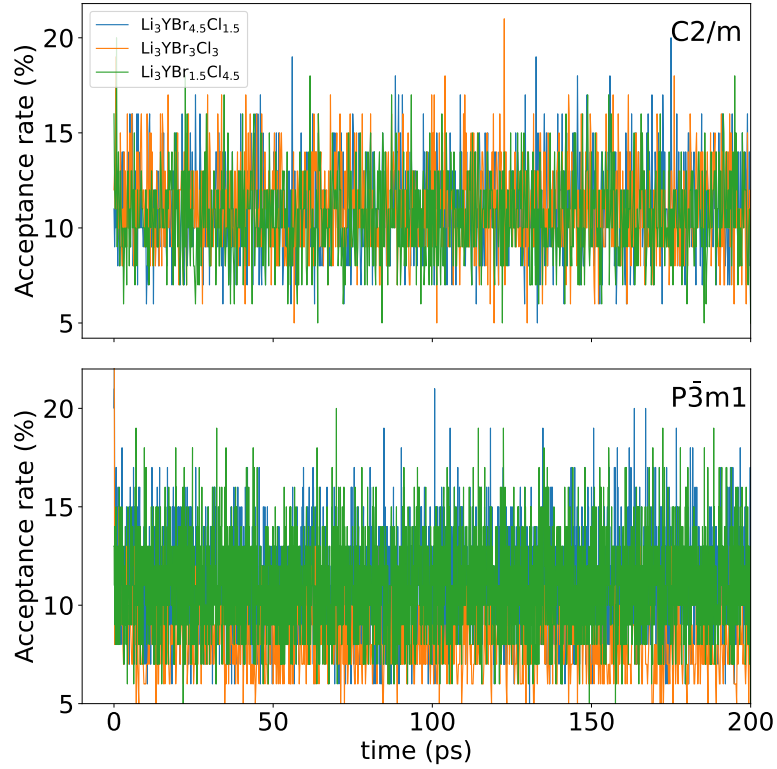


FIG. S3. Acceptance rate during the Monte Carlo simulations of LiYBr_{6(1-x)}Cl_{6x} in the C2/m (upper panel) and P $\bar{3}$ m1 (lower panel) phase at all the different compositions.

IV. RADIAL DISTRIBUTION FUNCTION OF STRUCTURE OF DIFFERENT MC SIMULATION

Fig. S4 shows the partial radial distribution functions (RDFs) for the 4 configurations of Li₃YBr₃Cl₃ in the P $\bar{3}$ m1 phase extracted from the MC simulation. The top panel shows the partial RDFs of the halogen atoms, while the lower panel shows the RDF between the Y and the halogen atoms. In all cases the RDFs for different snapshot are perfectly on top of each other, showing that different snapshots extracted from the MC simulations have the same structure.

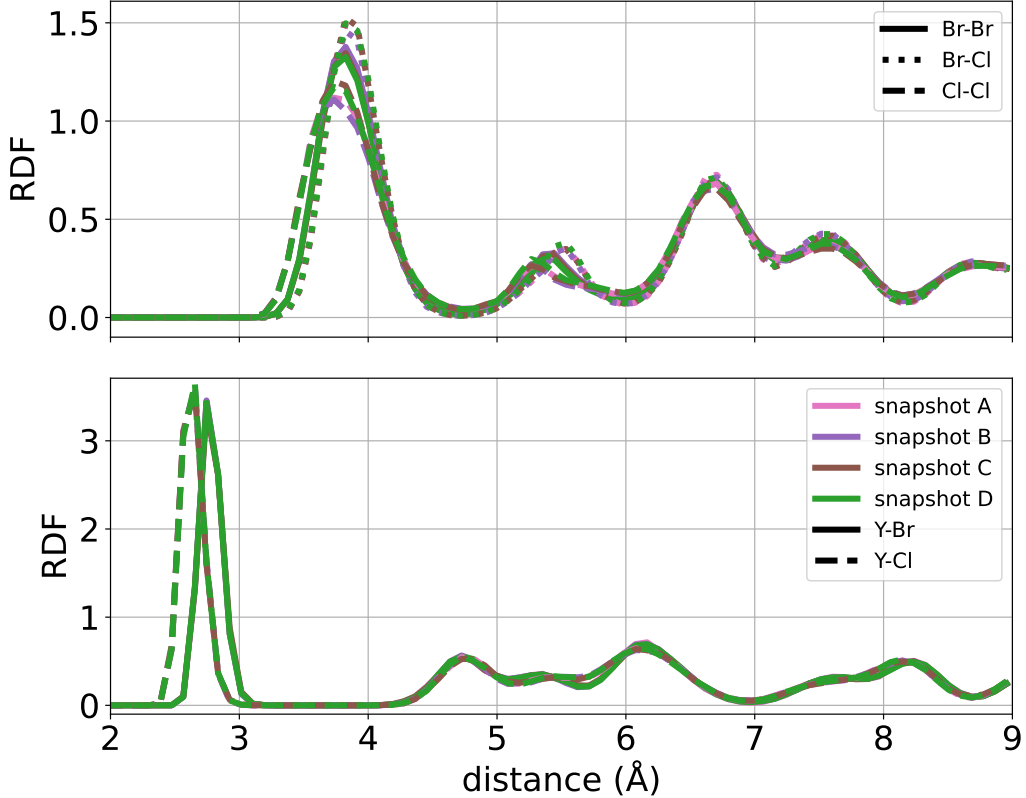


FIG. S4. Radial distribution functions (RDF) of 4 configuration of $\text{Li}_3\text{YBr}_3\text{Cl}_3$ in the $\text{P}\bar{3}\text{m}1$ phase. Upper panel contains the RDF between the different halogen atoms: Br-Br (continuous), Br-Cl (dotted), Cl-Cl (dashed). Lower panel contains the RDF between the Y atoms and the halogens: Y-Br (continuous), Y-Cl (dashed). These are extracted from the final 50 ps of 2 ns long NPT simulations.

V. EFFECTS OF ALLOYING ON THE CONDUCTIVITY

In the main text we show the effects of alloying on the conductivity showing, in the cases of mixed composition, the average conductivity of different snapshot at the same Br-Cl ratio. Fig. S5 is the equivalent of Fig. 5 in the main text, where for the mixed compositions each point correspond to the σ extracted from a simulation done with one of the structures selected from the MC simulation.

- [1] Zhantao Liu, Shuan Ma, Jue Liu, Shan Xiong, Yifan Ma, and Hailong Chen, “High Ionic Conductivity Achieved in $\text{Li}_3\text{Y}(\text{Br}_3\text{Cl}_3)$ Mixed Halide Solid Electrolyte via Promoted Diffusion Pathways and Enhanced Grain Boundary,” *ACS Energy Letters* **6**, 298–304 (2021).
- [2] Tetsuya Asano, Akihiro Sakai, Satoru Ouchi, Masashi Sakaida, Akinobu Miyazaki, and Shinya Hasegawa, “Solid Halide Electrolytes with High Lithium-Ion Conductivity for Application in 4 V Class Bulk-Type All-Solid-State Batteries,” *Advanced Materials* **30**, 1–7 (2018).
- [3] Eveline van der Maas, Wenxuan Zhao, Zhu Cheng, Theodosios Famprikis, Michel Thijs, Steven R. Parnell, Swapna Ganapathy, and Marnix Wagemaker, “Investigation of structure, ionic conductivity, and electrochemical stability of halogen substitution in solid-state ion conductor $\text{Li}_3\text{YBr}_x\text{Cl}_{6-x}$,” *The Journal of Physical Chemistry C* **127**, 125–132 (2023).

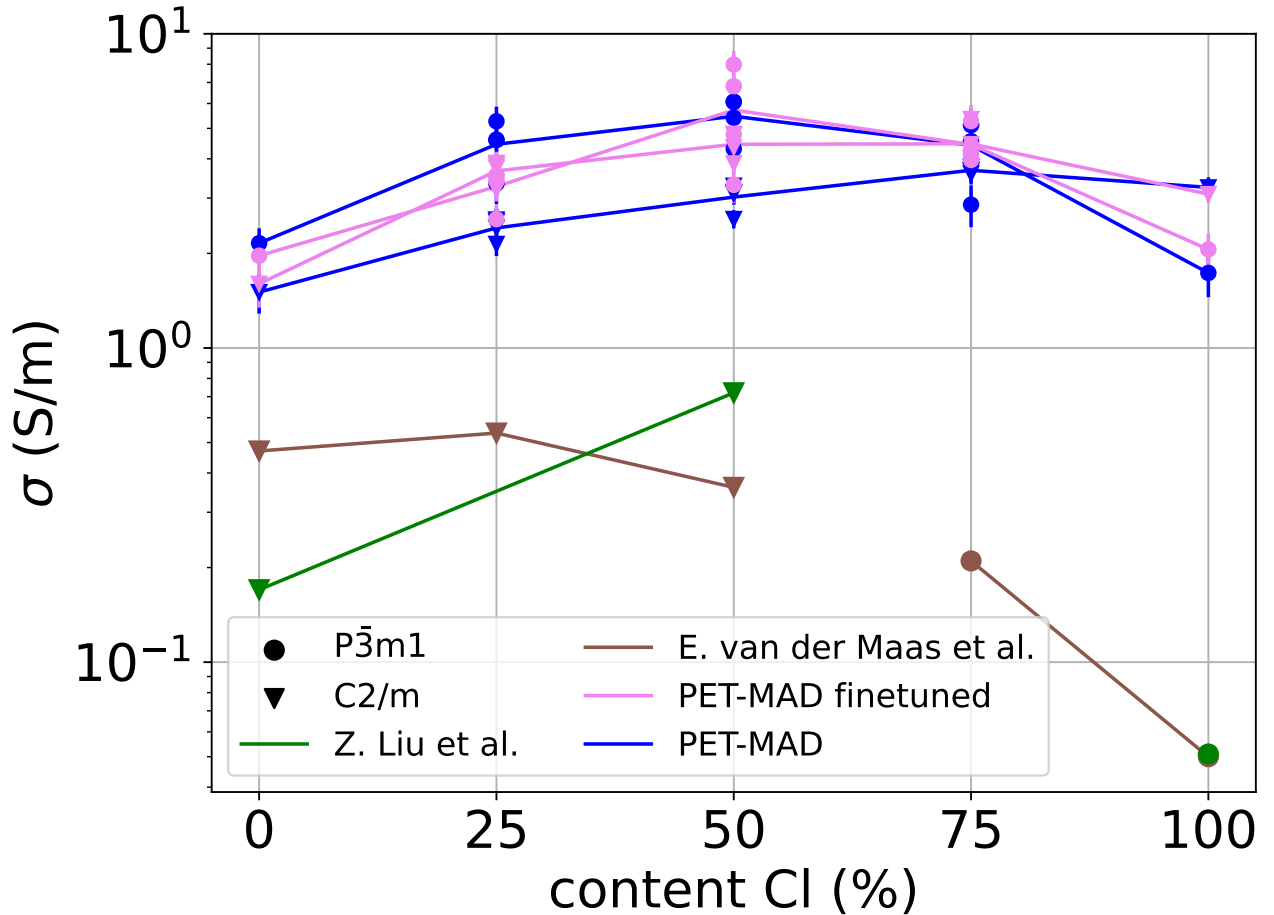


FIG. S5. Ionic conductivity (σ) of $\text{Li}_3\text{YBr}_{6(1-x)}\text{Cl}_{6x}$, with $x \in [0, 1]$, as a function of percentage of Cl content, computed via the PET-MAD universal potential (blue) and a PET model fine-tuned (pink line) on a specific dataset. Each point is the result of a calculation on a particular structure extracted from the MC procedure and the lines connects the average values as presented in Fig. 5 of the main text. Results are compared with experimental results reported in Ref. [1, 2] (green) and Ref. [3] (brown).

